BIOCELL

Tech Science Press

http://doi.org/10.32604/biocell.2026.075437

ARTICLE

Synergistic Cell Death: Cisplatin Inflames Tumors by Coordinating Multiple Death Programs

Ju Li[1], Pengcheng Rao[1], Dan Yang[1], Tong Zhou[1], Jianguo Gan[1], Die Lv[1], Shuting Zhou[1], Yang Peng[1], Xiaoqiang Xia[1], Qianming Chen[1], Yuchen Jiang[1], Jian Jiang[2], Xiaoping Xu[1,*] and Xiaodong Feng[1,*]

[1]State Key Laboratory of Oral Diseases & National Center for Stomatology & National Clinical Research Center for Oral Diseases & Frontier Innovation Center for Dental Medicine Plus & Research Unit of Oral Carcinogenesis and Management & Chinese Academy of Medical Sciences, West China Hospital of Stomatology, Sichuan University, Chengdu, China

[2]Department of Head and Neck Surgery, Sichuan Cancer Hospital and Institute, Sichuan Cancer Center, School of Medicine, University of Electronic Science and Technology of China, Chengdu, China

*Corresponding Authors: Xiaoping Xu. Email: xiaoping327@126.com; Xiaodong Feng. Email: xiaodongfeng@scu.edu.cn

Received: 31 October 2025; Accepted: 27 January 2026; Published: 13 May 2026

ABSTRACT: Objective: Multiple programmed cell death (PCD) pathways have been individually reported to be triggered by cisplatin, but whether and how they are co-regulated remains unclear. In this study, we comprehensively investigate the spectrum of cisplatin-induced PCD. **Methods:** We employed integrated *in vitro* and *in vivo* models, including human cancer cell lines, a Cal27 xenograft mouse model, and paired clinical specimens from an oral squamous cell carcinoma patient receiving neoadjuvant cisplatin-based chemotherapy. A comprehensive methodological suite-encompassing cell death assays, Western blotting, Hematoxylin and eosin staining, immunofluorescence, Cyclic multiplexed tissue staining, and pathway-specific pharmacological inhibitors was utilized to dissect the activation of apoptosis, necroptosis, pyroptosis, and ferroptosis. **Results:** Cisplatin simultaneously upregulates markers of PCD pathways (including apoptosis, necroptosis, pyroptosis, and ferroptosis) in a dose- or time-dependent manner. Pharmacological inhibition or genetic knockdown of key genes in each pathway significantly reduced cytotoxicity, confirming their functional roles. Notably, indicators of key pro-inflammatory death modalities, pyroptosis and ferroptosis, were prominently co-upregulated in both xenograft tumors and clinical patient samples, suggesting that these two forms of PCD may represent the predominant death forms in cisplatin-induced tumor cell death. **Conclusion:** Cisplatin induces the coordinated activation of multiple cell death programs within a unified framework. Prominent engagement of immunogenic cell death pathways, particularly pyroptosis and ferroptosis, provides a mechanistic basis for the clinically observed synergy between cisplatin and immune checkpoint blockade therapy.

KEYWORDS: Cisplatin; programmed cell death; pyroptosis; necroptosis; ferroptosis; apoptosis

1 Introduction

Cisplatin (DDP), a cornerstone platinum-based chemotherapeutic, received FDA approval in 1978 for testicular and bladder cancers. Its clinical utility rapidly expanded, establishing it as a front-line therapy, adjuvant treatment, or combination partner for diverse solid tumors, including those of the head and neck, lung, ovarian, and gastric organs [1–3]. Despite its broad efficacy, the clinical impact of cisplatin is significantly hampered by severe dose-limiting toxicities, including nephrotoxicity, ototoxicity, neurotoxicity, myelosuppression, and gastrointestinal distress, and the inevitable development of drug

resistance [4–7]. The therapeutic bottleneck arises because cisplatin's dual regulation of anticancer effects and toxicities is intrinsically linked to its fundamental role in cell death pathways, which is not yet fully deciphered. Consequently, elucidating cisplatin's modulation of cancer cell death mechanisms is critical for enhancing therapeutic efficacy and advancing rational combinatorial strategies.

The antitumor activity of cisplatin is classically attributed to its formation of DNA crosslinks with purine bases, which impedes DNA repair and triggers genomic instability. Historically, apoptosis, the first described form of programmed cell death (PCD), has been considered the primary mechanism driving cisplatin-induced cancer cell death [8]. However, the landscape of PCD has dramatically expanded since 1972, with the discovery and characterization of numerous distinct pathways, including necroptosis, pyroptosis, ferroptosis, neutrophil extracellular traposis (NETosis), parthanatos, lysosome-dependent cell death, autophagy-dependent cell death, alkaliptosis, oxeiptosis, and the more recently identified cuproptosis and disulfidptosis [9–11]. Interestingly, emerging evidence suggests that cisplatin may also sporadically engage non-apoptotic PCD pathways, with evidence from isolated reports linking cisplatin exposure to necroptosis [12,13], pyroptosis [14], and ferroptosis [15,16]. Nevertheless, a systematic investigation into the full spectrum of cisplatin-induced PCD, termed "multiple-PCD" (multi-PCD), and the interplay between these pathways is lacking. This knowledge gap represents a significant limitation, as a comprehensive understanding of cisplatin's capacity to engage diverse PCD mechanisms holds strong potential for elucidating its full therapeutic mechanism, explaining resistance phenotypes, and devising strategies to amplify its efficacy.

Therefore, this study aims to investigate the spectrum of cisplatin-induced multi-PCD through the integration of four PCD pathways within a unified experimental and clinical framework, thereby providing new theoretical insights for elucidating the antitumor mechanism of cisplatin, overcoming clinical drug resistance, and optimizing immunochemotherapeutic strategies.

2 Materials and Methods

2.1 Drugs and Antibodies

Cisplatin (HY-17394) and ferrostatin-1 (Fer-1, HY-100579) were procured from MedChem Express (Princeton, NJ, USA), necrosulfonamide (NSA, S8251) and Z-LEHD-FMK TFA (zLEHD, S7313) were obtained from Selleck Chemical (Houston, TX, USA). These compounds were utilized as pharmacological inhibitors targeting distinct cell death pathways. Ferrostatin-1 is a potent and selective inhibitor of ferroptosis, an iron-dependent form of regulated cell death characterized by lipid peroxidation. Necrosulfonamide effectively blocks necroptosis, a form of programmed necrosis, by inhibiting the downstream executioner MLKL. Z-LEHD-FMK is a specific caspase inhibitor that primarily targets caspase-9, thereby inhibiting the intrinsic (mitochondrial) apoptotic pathway.

The main antibodies used in the western blot and immunoprecipitation experiments were as follows: anti-γ-H2AX (#80312), anti-cleaved PARP (#9541), anti-cleaved caspase-3 (#9661), anti-cleaved caspase-7 (#9491), anti-caspase-9 (#9502), and anti-RIP3 (#15828) were purchased from Cell Signaling Technology (CST, Danvers, MA, USA); anti-phospho-MLKL (ab187091), anti-phospho-RIP3 (#ab209384), anti-GSDME (ab215191), anti-GSDMD (ab219800), and 4-hydroxynonenal (4-HNE) (ab46545) were purchased from Abcam (Waltham, MA, USA); anti-β-actin (sc-69879) was purchased from Santa Cruz Biotechnology (Dallas, TX, USA); anti-Ki67 (HA721115), and anti-MLKL (ET1601-25) were purchased from HUABIO (Hangzhou, China); anti-GAPDH (BA2913) was purchased from Boster (Wuhan, China). The secondary antibodies, including anti-rabbit IgG (HA1001) and anti-mouse IgG (HA1006), were purchased from HUABIO (Hangzhou, China).

2.2 Cell Culture

CAL27 and HCT15 cells were purchased from the China Center for Type Culture Collection (Wuhan, China). The CAL27 cell line was cultured in high-glucose DMEM (Invitrogen, Thermo Fisher Scientific, Waltham, MA, USA) supplemented with 10% fetal bovine serum (Gibco, Thermo Fisher Scientific) and 1% penicillin/streptomycin (Thermo Fisher Scientific, Waltham, MA, USA). The HCT15 cells were cultured in Roswell Park Memorial Institute (RPMI) 1640 medium (Thermo Fisher Scientific, Waltham, MA, USA) supplemented with 10% fetal bovine serum and 1% penicillin/streptomycin. Prior to utilization, all cell lines underwent authentication via short tandem repeat (STR) profiling and were verified to be devoid of mycoplasma contamination.

2.3 Immunofluorescence

CAL27 cells were seeded on glass coverslips in a 24-well plate at a density of 30–40% confluence and treated with cisplatin at concentrations of 0 μM, 2 μM, 4 μM, 8 μM, and 16 μM for 48 h. After treatment, the cells were washed 3 times with 1× phosphate-buffered saline (PBS, pH 7.2, BL302A, Biosharp, Hefei, China). After fixation with 4% paraformaldehyde (PFA) in PBS for 30 min at room temperature (RT), the cells were washed 3 times with PBS and permeabilized with 0.5% Triton X-100 with 200 mM glycine in PBS for 10 min. The coverslips were subsequently quickly washed 3 times in PBS and blocked with 5% normal goat serum (blocking buffer) for 1 h at RT before incubation with γ-H2AX antibody (1:200, CST, 80312S) diluted in 0.1% blocking buffer overnight at 4°C. The coverslips were subsequently washed 3 times in PBS, followed by incubation with a secondary antibody labeled with Alexa Fluor 594 (1:1000, A11020, Thermo Fisher Scientific, Waltham, MA, USA) in 0.1% blocking buffer for 1.5 h at RT in the dark. The cells were washed 3 times in PBS and mounted with ProLong® Gold Antifade Reagent with DAPI-Special Packaging (P36935, Thermo Fisher Scientific, Waltham, MA, USA). Finally, the images were observed and acquired with an Olympus VS200 whole slide scanner (Model: VS200, Olympus Corporation, Tokyo, Japan). Image analyses were carried out with Fiji (an open-source image processing package based on ImageJ, version 2.1.0/1.53c).

2.4 Cell Death Assay

The percentage of dead cells was assessed by a Calcein/PI Cell Viability/Cytotoxicity Assay Kit (C2015, Beyotime, Shanghai, China) following the manufacturer's instructions. Briefly, CAL27 cells were seeded in a 24-well plate at a density of 30–40% confluence and treated with cisplatin at concentrations of 0 μM, 2 μM, 4 μM, 8 μM, and 16 μM or inhibitor drugs (zLEHD at 5 μM, NSA at 1 μM, and Fer-1 at 10 μM) for a specified period (See figure legend). And the inhibitory effect of Fer-1 was further confirmed in the HCT15 cell line. Additionally, pyroptosis was specifically assessed in GSDME-knockdown CAL27 cells under conditions of cisplatin treatment (0 μM, 8 μM, or 16 μM for 36 h). After treatment, the cells were gently washed with 1× PBS (0.01 M, pH 7.4), and an appropriate volume of calcein AM/PI detection working solution was added. Cells were then incubated at 37°C in the dark for 30 min. The cells were labeled with propidium iodide (PI) and calcein AM. Calcein AM stains live cells and emits green fluorescence, whereas PI stains dead cells and emits red fluorescence. Images were captured using EVOS M5000 microscope (Model No. EVOS M5000, Invitrogen, USA), and statistical analysis and plotting were performed using Count_Debug 1.0.2.1 (a custom in-house software at the NIH, was used for manual cell counting) and GraphPad Prism 9.0 software (San Diego, CA, USA; www.graphpad.com).

2.5 Apoptosome Staining

CAl27 cells were seeded in 24-well plates at 30–40% confluence and treated with cisplatin (0, 2 μM, 4 μM, 8 μM, and 16 μM). After 48 and 72 h, cells were stained with Vybrant DyeCycle Green (V35004, Thermo Fisher Scientific, Waltham, MA, USA) according to the manufacturer's instructions. Fluorescent images of the apoptosome were captured using an EVOS M5000 microscope. Quantitative analysis was performed with GraphPad Prism 9.0 software.

2.6 siRNA Transfection

Small interfering RNAs (siRNAs) targeting *gasdermin E* (siRNA, GGUCCUAUUUGAUGAUGAA) and were siNC (non-targeting control, UUCUCCGAACGUGUCACGUTT) procured from RiboBio (Guangzhou, China). Transfection was carried out by Lipofectamine RNAiMAX Transfection Reagent (#13778150, Thermo Fisher Scientific, Waltham, MA, USA) according to the manufacturer's instructions. For siRNA transfection, GSDME-targeting siRNA was used for the experimental group, while an NC siRNA served as the control. Briefly, 10 μL of siRNA and 7.5 μL of Lipofectamine RNAiMAX transfection reagent were each diluted in separate 1.5 mL microcentrifuge tubes containing 100 μL of Opti-MEM medium. The two solutions were then combined into one tube, gently vortexed, briefly centrifuged (1000 rpm, 20 s, Eppendorf Centrifuge 5702, Eppendorf SE, Hamburg, Germany), and incubated at room temperature for 5 min to allow complex formation. CAL27 cells were seeded at 30% confluence directly into the prepared siRNA-lipid complex mixture. The cell suspension was gently mixed and plated into one well of a 6-well plate, followed by incubation at 37°C. After cell attachment, cisplatin was added directly to the culture medium at final concentrations of 0 μM, 8 μM, or 16 μM. The cells were then cultured at 37°C for an additional 24–72 h before being harvested for subsequent cell death assays and Western blot analysis. CAL27 cells were harvested 36 h post-siRNA transfection for Western blot analysis.

2.7 Western Blot

Whole-cell extracts from CAL27 and HCT15 cells were prepared using RIPA lysis and extraction buffer (#89900, Thermo Fisher Scientific, Waltham, MA, USA) supplemented with protease inhibitor (P1005, Beyotime, Shanghai, China) and phosphatase inhibitor (HY-K0022, Beyotime, Shanghai, China). The lysates were boiled in protein loading buffer with sodium dodecyl sulfate (SDS) at 95°C for 10 min. Protein samples were resolved by 10%, 12.6%, or 15% SDS-PAGE gel and transferred to positively charged PVDF membranes (Millipore, Billerica, MA, USA). After being blocked with 5% skim milk in 1× TBST (25 mM Tris [pH 7.6],138 mM NaCl, and 0.05% Tween-20) for 1 h, the membranes were incubated with primary antibodies at 4°C overnight. The next day, the membranes were washed 3 times in 1× TBST, followed by incubation with secondary antibodies at RT for 1 h. Immunoblots were performed with the following antibodies: anti-γ-H2AX, anti-cleaved PARP, anti-cleaved caspase-3 (1:1000, all from CST, USA), anti-cleaved caspase-7, anti-caspase-9 (1:2000, both from CST, USA), anti-MLKL (1:3000, HUABIO, China), anti-phospho-MLKL, anti-GSDME, anti-GSDMD (1:1000, all from Abcam, USA), anti-β-actin (1:3000, Santa Cruz Biotechnology, USA), and anti-GAPDH (1:2000, Boster, China). HRP-conjugated secondary antibodies: anti-rabbit (1:20,000; HUABIO, China) and anti-mouse (1:20,000; HUABIO, China) were used for signal detection by Immobilon chemiluminescent HRP substrate (WBKLS0500, Millipore, Billerica, MA, USA) with a Bio-Rad bioluminescence device (Model No. ChemiDoc TM MP Imaging System, BIO-RAD, Hercules, CA, USA). Western blot results were normalized against internal reference proteins (β-actin or GAPDH).

2.8 ROS Measurement

The intracellular ROS level was assessed by the Reactive Oxygen Species Assay Kit (S0033S, Beyotime, Shanghai, China) following the manufacturer's instructions. CAL27 cells were cultured in confocal dishes overnight and then treated with 0 μM, 2 μM, 4 μM, 8 μM, or 16 μM cisplatin. 48 h later, cells were washed 3 times with 1× PBS (0.01 M, pH 7.4) and stained with 50 μM 2,7-Dichlorodi-hydrofluorescein diacetate (DCFH-DA) and 1× Hoechst 33342 (P0133, Beyotime, Shanghai, China) for 30 min at 37°C in the dark. Images were acquired using an Olympus confocal laser scanning microscope (Model No. FV3000RS, Olympus, Tokyo, Japan).

2.9 Lipid Peroxidation Measurement

Lipid peroxidation was measured using the Lipid Peroxidation Probe BDP 581/591 C11 (D3861, Thermo Fisher Scientific, Waltham, MA, USA) according to the manufacturer's instructions. CAL27 cells were seeded in confocal dishes and incubated at 37°C overnight. After different treatments, cells were washed 3 times in 1× PBS (0.01 M, pH 7.4), stained with 1 μM BDP 581/591 C11 at 37°C for 30 min, washed 3 times in HBSS (BL561A, Biosharp, Hefei, China), and imaged using an Olympus FV3000 confocal laser scanning microscope.

2.10 Animal Experiments

All animal studies were conducted in accordance with ethical guidelines and were approved by the Experimental Animal Ethics Committee of West China Hospital, Sichuan University (Ethics Approval No. 20220330002). Female 5-week-old NU/NU mice were purchased from Charles River CHN (Beijing, China). After one week of acclimation, a xenograft model was established by subcutaneously injecting CAL27 cells (1.5×10^6 cells per injection) into both flanks of 6-week-old NU/NU mice. Tumor volume and mouse body weight were measured every 3–4 days using the formula $(length \times width^2)/2$ to calculate tumor volume, where length and width represent the maximum length and width of the tumor. Once tumors reached a volume of 100 mm^3, the mice were randomly divided into three groups with five mice in each group: (1) vehicle, (2) 1 mg/kg cisplatin, and (3) 4 mg/kg cisplatin, intraperitoneal injection twice a week. The experimental endpoint was defined as the day when the untreated control group tumor reached a size of approximately 1000 mm^3. All animals were housed in appropriate sterile filter-capped cages and provided with a normal mouse growth diet. Mice were euthanized at the indicated time points, and tumors were harvested for histological analysis and immunohistochemistry evaluation.

2.11 Hematoxylin and Eosin (H&E) Staining

The tissue samples collected in Method 2.10 were fixed in 4% paraformaldehyde, paraffin-embedded, and sectioned at 4 μm. After baking at 65°C for 2–3 h, sections were deparaffinized in xylene (#1330-20-7, Chron Chemicals, Chengdu, China; two changes, 2 min each) and rehydrated through a graded ethanol series (100%, 95%, 70%; 2 min each). Following a 2-min tap water rinse, sections were stained with hematoxylin (#ZLI-9610, ZSGB-BIO, Beijing, China; 3 min), rinsed, counterstained with eosin (2 min), dehydrated through ethanol, cleared in xylene, and mounted.

2.12 Immunohistochemistry

Immunohistochemical (IHC) staining was conducted according to established protocols [10,11]. The mouse tumor tissue was fixed with 4% PFA, embedded in paraffin, and cut at a thickness of 4 μm. After being

baked at 65°C for 2 h, the samples were gradually dewaxed in xylene (100%, #1330-20-7, chronchemicals, Chengdu, China) and rehydrated in a graded series of alcohols (100%, 95%, 70%; 2 min each). The tumor samples were treated with 3% H_2O_2 for 10 min at RT to inhibit endogenous peroxidase activity, followed by antigen retrieval using a pressure cooker for 5 min. The samples were then washed gently 3 times with 1× PBS (0.01 M, pH 7.4) before being incubated overnight at 4°C with Ki67 (1:300), γ-H2AX (1:300), cleaved caspase-3 (1:300), cleaved caspase-7 (1:300), pMLKL (1:200), GSDME (1:200), and 4-hydroxynonenal (4-HNE) (1:200) antibodies. The next day, the slides were applied to equilibrate to room temperature for 30 min, washed 3 times with PBS, and incubated with secondary antibodies at RT for 1 h. Following another round of washing 3 times with PBS, DAB (#GK347010, Gene Tech, Shanghai, China) color development and hematoxylin (#ZLI-9610, ZSGB-BIO, Beijing, China) counterstaining were performed. The DAB working solution was prepared by adding approximately one drop of DAB chromogen per milliliter of substrate buffer. After mixing, it was applied to the tissue sections and developed at room temperature for 3–10 min. Following development, the sections were counterstained with hematoxylin for 3–10 min at room temperature. Sections were then dehydrated, cleared in xylene, and mounted. Finally, the stained slides were scanned using a Leica scanner (Model No. ImageScope, Leica Biosystems, Waltham, MA, USA) and subjected to quantitative analysis.

2.13 Clinical Specimens

The clinical samples used in this study were obtained from one patient with oral squamous cell carcinoma (OSCC) who was treated in the Department of Head and Neck Surgery at Sichuan Cancer Hospital and Institute. The patient received two cycles (Each cycle lasts 30 days) of neoadjuvant chemotherapy (NAC) with the following regimen: docetaxel (95 mg, intravenous infusion, day 1) combined with cisplatin (30 mg, intravenous infusion, days 1–3). A systematic Cyclic multiplexed tissue staining (CmTSA) was conducted on matched pre-NAC and post-NAC clinical specimens. The study received approval from the Ethics Committee for Medical Research and New Medical Technology of Sichuan Cancer Hospital (Ethics Approval No. KY-2021-001-06); written informed consent was required of and obtained from all patients.

2.14 Cyclic Multiplexed Tissue Staining (CmTSA) and Analysis Strategy

Cyclic multiplexed tissue staining (CmTSA) and analysis strategy were performed essentially as previously described [17]. These experiments were conducted at Chengdu Minghong Tiancheng Biotechnology company (Chengdu, China), experimental workflow is illustrated in Fig. S1. Briefly, clinical specimens along with pre-NAC and post-NAC oral squamous cell carcinoma (OSCC) samples were processed to phenotype and enumerate multi-PCD events using the IRISKit® HyperView mTSA Kit (#MH010101, Chengdu Minghong Tiancheng Biotechnology Co., Ltd., Chengdu, China) (Fig. S1).

Sections underwent deparaffinization in xylene, rehydration through graded ethanol, and antigen retrieval in preheated pH 9.0 EDTA buffer (95°C, 30 min). For CmTSA, background fluorescence was first quenched using the IRISKit® HyperView system (#MH030101, Chengdu Minghong Tiancheng Biotechnology Co., Ltd., Chengdu, China). Staining was performed iteratively using the IRISKit® HyperView multiplex kit (#MH010101): each cycle involved sequential incubation with a primary antibody, an HRP-conjugated secondary antibody, and a tyramide-based fluorophore (DAPI, FITC, Cy3, or Cy5), followed by antibody stripping. Primary antibodies used were: anti-4-HNE (ferroptosis marker; dilution 1:200; Abcam, USA), anti-GSDME (pyroptosis marker; dilution 1:200; Abcam, USA), anti-γ-H2AX (DNA damage marker; dilution 1:100; HUABIO, China). anti-cleaved caspase-7 (apoptosis marker; dilution 1:100; CST, USA), anti-cleaved caspase-3 (apoptosis marker; dilution 1:100; CST, USA), anti-Ki67 (cell proliferation marker; dilution

1:3000; HUABIO, China). anti-pancytokeratin (panCK, epithelial cell marker; HA601138, dilution 1:2000; HUABIO, China), anti-MLKL (necroptosis marker; dilution 1:200; HUABIO, China). Between cycles, specific fluorescence was quenched while preserving DAPI for image registration. Slides were imaged at 20 × magnification (EVIDENT VS200, Evident Scientific Inc., Waltham, MA, USA), and multi-round images were aligned using rigid transformation in Fiji based on DAPI features. We performed whole-slide scanning using the Evident VS200 system and generated comprehensive 8-plex 9-color composite images by integrating all fluorescent channels. In the QuPath version 0.5.1 software (University of Edinburgh, Edinburgh, Scotland, UK), a threshold range of 0–255 was applied to the panCK channel to specifically identify and delineate regions of epithelial-derived malignant tumor cells. Within the same delineated tumor region, single-channel images of the other markers were exported for further analysis. Individual cells were then manually annotated and numbered in Photoshop CS6 software (Adobe Systems Incorporated, San Jose, CA, USA) based on DAPI nuclear staining, and each cell was classified as marker-positive or marker-negative according to the expression of four distinct cell death-related markers. The subtype of cell death was determined by the co-expression pattern of these markers: expression of one marker was defined as single-type cell death, two markers as dual-type, three markers as triple-type, and all four markers as quadruple-type cell death. For quantification, approximately 200 cells per image were evaluated across more than five fields per slide to ensure representative sampling. The percentage of positive cells for each death subtype was calculated, and statistical analysis was performed using GraphPad Prism 9.0 software (www.graphpad.com). The detailed workflow is shown in Fig. S1A,B.

2.15 Statistical Analysis

The data are presented as mean ± Standard Error of the Mean (SEM) from three independent experiments, with the exception of the precious clinical samples, which, due to their limited availability, were analyzed in a single experiment. At least three independent experiments were conducted with consistent results for the non-clinical data, and representative results are shown.

Statistical analysis was performed using GraphPad Prism software (version 9.0.0, GraphPad Software, La Jolla, CA, USA). Prior to selecting statistical tests, the normality of data distribution for each experimental group was assessed using the Shapiro-Wilk test. For datasets that met the normality assumption, the appropriate parametric test was applied: Student's two-tailed *t*-test for comparisons between two groups, or one-way analysis of variance (ANOVA) followed by Dunnett's post hoc test for multiple comparisons, as indicated in the figure legends. For datasets that did not meet the normality assumption, the corresponding non-parametric tests were employed: the Mann-Whitney U test for two-group comparisons, or the Kruskal-Wallis test followed by Dunn's post hoc test for multiple comparisons. This approach ensures the validity of all statistical inferences in the study. In all cases: n.s. $p > 0.05$; $^{*}p < 0.05$; $^{**}p < 0.01$; $^{***}p < 0.001$.

3 Results

3.1 Cisplatin Induces Dose- and Time-Dependent DNA Damage and Cell Death

To achieve the aim of this study, we selected the Cal27 (oral squamous cell carcinoma) and HCT15 (colorectal carcinoma) cell lines, as they represent two major cancer types where cisplatin is a first-line therapy, ensuring clinical relevance and allowing us to test the generality of our findings. The cisplatin concentrations used were informed by clinically achievable plasma levels and prior studies [3,18,19], ensuring physiological and pharmacological relevance for a systematic investigation into cisplatin-induced multi-PCD.

Consistent with its established mechanism, cisplatin exerts cytotoxicity primarily through DNA crosslinking, inducing DNA damage that triggers cell death. To quantitatively assess cisplatin-induced DNA damage, we monitored phosphorylation of histone H2AX (γ-H2AX), a well-established molecular marker of DNA double-strand breaks and activation of the DNA damage response (DDR) [20]. Immunofluorescence analysis in CAL27 cells revealed a significant, dose-dependent increase in γ-H2AX foci formation following 48-h treatment with cisplatin (0 μM, 2 μM, 4 μM, 8 μM, 16 μM) (Fig. 1A). Quantification confirmed that the mean fluorescence intensity of γ-H2AX escalated progressively with increasing cisplatin concentration (Fig. 1B). This dose-dependent induction of DNA damage was further validated by immunoblotting, which showed a corresponding increase in γ-H2AX protein levels (Fig. 1C).

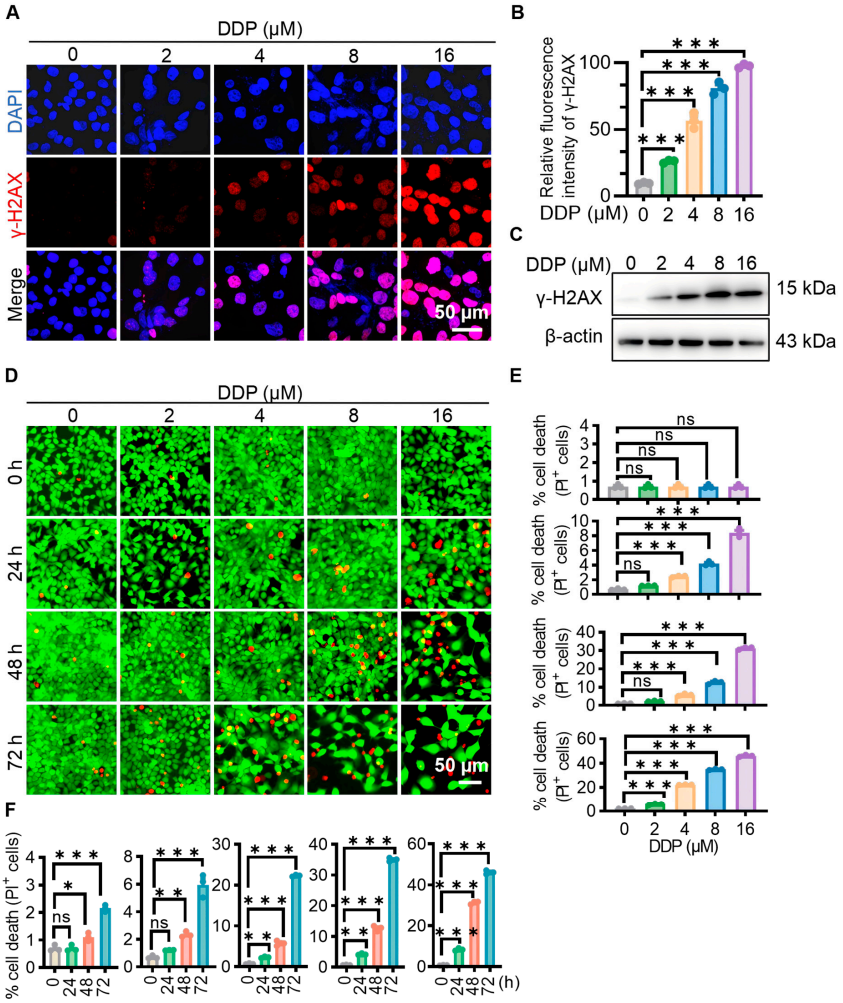

Figure 1: Cisplatin induces DNA damage and cell death. (**A**) Immunofluorescence staining of γ-H2AX (red) and Hoechst staining for nuclear DNA (blue) in CAL27 cells after cisplatin treatment. Scale bar, 50 μm. (**B**) Quantitative analysis of DNA damage frequency based on γ-H2AX staining. The Fluorescence intensity was greater than that of the control group, and the red color represents positive cells. $^{***}p < 0.001$ (one-way ANOVA with multiple comparisons, n = 3). (**C**) DNA damage was measured by immunoblotting, and β-actin was used as the internal control. (**D**) Cell death was measured with a Calcein/PI Cell Viability/Cytotoxicity Assay Kit, and live and dead cells are shown in green and red, respectively. Scale bar, 50 μm. (**E**,**F**) Quantitative analysis of the cell death rate based on Calcein/PI Cell Viability/Cytotoxicity Assay Kit. n.s. $p > 0.05$, $^{*}p < 0.05$, $^{**}p < 0.01$, $^{***}p < 0.001$ (one-way ANOVA multiple comparisons test, n = 3). Cells treated with the vehicle were used as controls.

We next evaluated cisplatin-induced cell death over time using a dual Calcein-AM/PI viability assay (Fig. 1D). Calcein-AM labels live cells (green fluorescence), while propidium iodide (PI) penetrates dead/damaged cells (red fluorescence). Treatment with cisplatin resulted in a clear time- and dose-dependent increase in cell death (Fig. 1E,F). Representative images illustrate the shift from predominantly viable (green) cells in controls to increasing PI-positive (red) cells with higher cisplatin doses and longer exposure times (Fig. 1E,F). Importantly, a direct relationship between early DNA damage and subsequent cell death was observed: higher cisplatin concentrations induced greater γ-H2AX signal at 48 h (Fig. 1A–C), correlating with increased cell death detected at the same timepoint (Fig. 1D–F). Furthermore, extending treatment duration significantly amplified cell death, particularly evident at 72 h across all concentrations tested (Fig. 1E,F). Collectively, these results demonstrate that cisplatin potently induces DNA damage and subsequent cell death in a highly concentration- and time-dependent manner in CAL27 cells.

3.2 Cisplatin Induces Caspase-Dependent Apoptosis in a Dose- and Time-Dependent Manner

While cisplatin triggers multiple forms of cell death (as explored subsequently), apoptosis remains a well-established primary mechanism. Apoptosis proceeds through extrinsic (death receptor) or intrinsic (mitochondrial) pathways, converging on caspase activation [11,21]. Initiator caspases (e.g., caspase-8/-9/-10) propagate death signals, while effector caspases (e.g., caspase-3/-6/-7) execute cellular dismantling [22,23]. Immunoblot analysis revealed that cisplatin treatment induced a pronounced, concentration-dependent upregulation of key apoptotic effector proteins in CAL27 cells. Specifically, levels of cleaved PARP, cleaved caspase-9, cleaved caspase-3, and cleaved caspase-7 were significantly elevated following cisplatin exposure (Fig. 2A). This dose-dependent activation of core apoptotic executioners was corroborated in HCT15 cells (Fig. 2B), demonstrating broad relevance across tumor cell lines. Given that cisplatin-induced DNA damage primarily activates the intrinsic (mitochondrial) apoptosis pathway, we employed Z-LEHD-FMK TFA (zLEHD), a specific caspase-9 inhibitor, for functional validation. Pretreatment with zLEHD significantly attenuated cisplatin-induced cell death in a dose-response assay (Fig. 2C), directly implicating caspase-9-dependent intrinsic apoptosis. Consistent with caspase activation, cisplatin treatment induced hallmark morphological changes of apoptosis. Staining revealed a dose- and time-dependent increase in apoptotic bodies (Fig. 2D,E). Significant increases were observed at 48 h for 8 μM and 16 μM cisplatin, and by 72 h, even the 2 μM dose elicited a significant elevation compared to controls (Fig. 2E). Furthermore, immunofluorescence analysis confirmed that zLEHD markedly reduced cisplatin-induced cell death (Fig. 2F,G), reinforcing the critical contribution of caspase-9-mediated apoptosis. This protective effect aligns mechanistically with the observed reduction in cell death quantified functionally (Fig. 2C). Collectively, these results demonstrate that cisplatin potently activates the intrinsic apoptotic pathway, characterized by caspase-9, -3, and -7 cleavage and PARP activation, culminating in characteristic morphological changes. Critically, pharmacological inhibition of caspase-9 significantly blunts cisplatin cytotoxicity, establishing its essential role in this cell death modality.

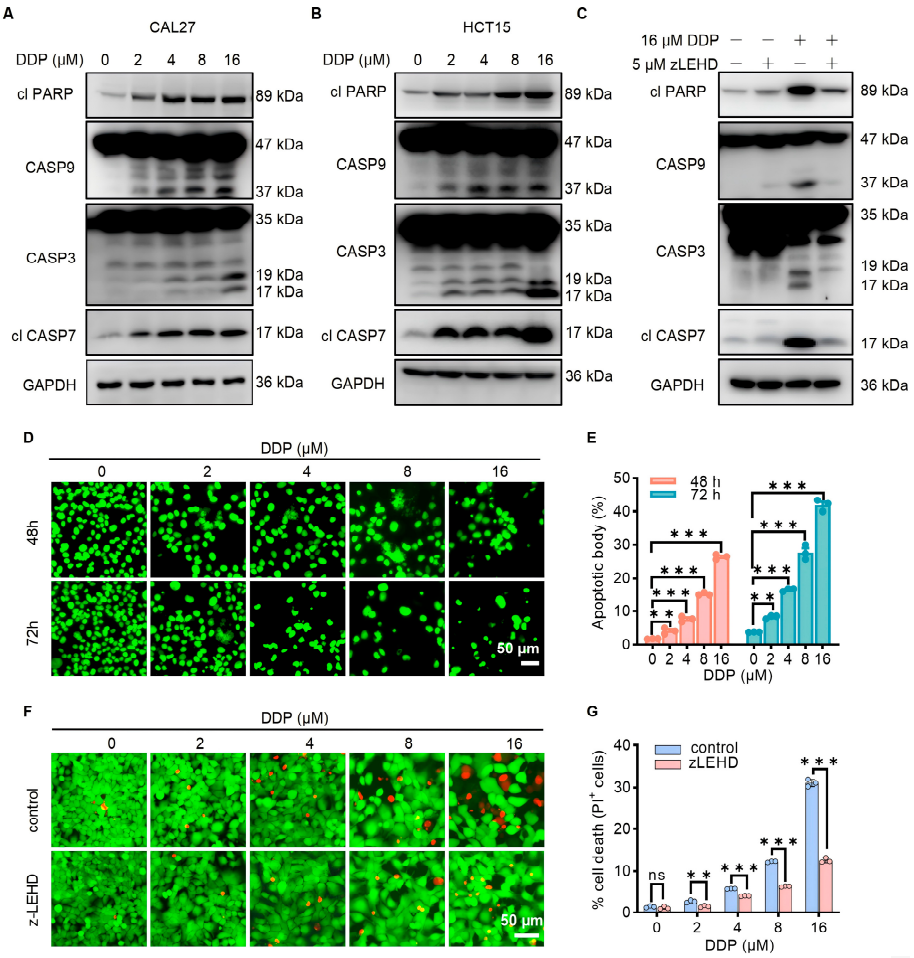

Figure 2: Cisplatin induces apoptosis. (**A**,**B**) Immunoblot analysis of cleaved (P89) PARP (cl PARP), pro-(P47) and cleaved (P37) caspase-9 (CASP9), pro-(P35) and cleaved (P17/P19) caspase-3 (CSAP3), cleaved (P20) caspase-7 (cl CASP7) in CAL27 cells (**A**) and HCT15 cells (**B**) after cisplatin treatment (48 h). (**C**) Immunoblotting was performed to assess the protein levels of caspase-9, caspase-3, and cleaved caspase-7 in CAL27 cells. Cells were pretreated with 5 μM zLEHD for 2 h and subsequently treated with or without 16 μM cisplatin for an additional 48 h. (**D**,**E**) Apoptosome staining and quantification by Vybrant Dye-Cycle TM Green and Count_Debug, respectively. Scale bar, 50 μm. $^{**}p < 0.01$, $^{***}p < 0.001$ (one-way ANOVA multiple comparisons test, n = 3). (**F**) Representative images of cell death after treatment with 0 μM, 2 μM, 4 μM, 8 μM, or 16 μM cisplatin in the presence or absence of a caspase-9 inhibitor, 5 μM zLEHD, for 48 h. The red and green signals mark dead and live cells, respectively. Scale bar, 50 μm. (**G**) Quantification of cell death in F. n.s. $p > 0.05$, $^{**}p < 0.01$, $^{***}p < 0.001$ (student's t test, n = 3).

3.3 Cisplatin Triggers Necroptosis through RIPK3-MLKL Pathway Activation

Beyond apoptosis, we investigated cisplatin's capacity to induce necroptosis: a caspase-independent programmed cell death pathway mediated by RIPK3 (receptor-interacting protein kinase 3) and MLKL (mixed lineage kinase domain-like protein). Necroptosis initiation requires RIPK3 activation, which subsequently phosphorylates MLKL, leading to plasma membrane disruption and lytic cell death. Phosphorylation of MLKL at human-specific sites (T357/S358) serves as a key molecular marker of pathway activation [24]. Immunoblot analysis revealed that cisplatin treatment induced a concentration-dependent activation of the necroptotic pathway in CAL27 cells. Phosphorylation of both RIPK3 and MLKL (at S358) was significantly upregulated at higher cisplatin concentrations (8 μM and 16 μM), while total MLKL levels remained stable

(Fig. 3A,B). This demonstrates direct engagement of the core necroptotic machinery. To functionally validate necroptosis induction, we employed the MLKL-specific inhibitor necrosulfonamide (NSA). Pharmacological inhibition of MLKL significantly attenuated cisplatin-induced cell death (Fig. 3C,D), confirming the functional contribution of necroptosis to cisplatin's cytotoxicity. Collectively, these results demonstrate that cisplatin activates canonical necroptotic signaling through RIPK3-dependent phosphorylation of MLKL at S358, contributing to cell death, particularly at higher therapeutic concentrations.

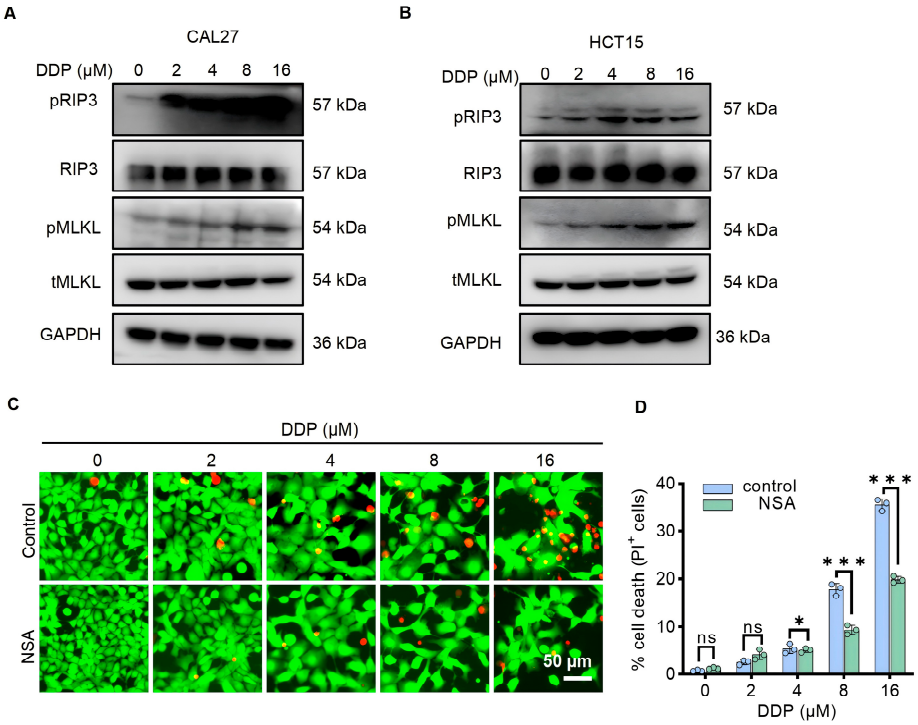

Figure 3: Cisplatin induces Necroptosis. (**A**,**B**) Necroptosis-related proteins, including phospho-RIP3 (pRIP3), phospho-MLKL (pMLKL) and total MLKL (tMLKL) were detected by western blotting in CAL27 cells (**A**) and HCT15 cells (**B**) after cisplatin treatment (24 h). (**C**) Cell death was assessed in CAL27 cells treated with 0 μM, 2 μM, 4 μM, 8 μM, or 16 μM cisplatin in the presence or absence of a MLKL-specific inhibitor, 1 μM necrosulfonamide (NSA), for 48 h. Red indicates dead cells, while green represents live cells. Scale bar, 50 μm. (**D**) Quantification of cell death from C. n.s. $p > 0.05$, $^{*}p < 0.05$, $^{***}p < 0.001$ (student's t test, n = 3).

3.4 Cisplatin Induces Pyroptosis through Caspase-3-Mediated GSDME Cleavage

Beyond apoptosis and necroptosis, we investigated cisplatin's potential to trigger pyroptosis, a lytic form of programmed cell death executed by gasdermin family proteins, leading to plasma membrane permeabilization [25]. While gasdermin D (GSDMD) is a well-characterized pyroptosis effector, immunoblot analysis revealed no detectable cleavage of GSDMD in cisplatin-treated CAL27 cells (Supplementary Fig. S2A,B). Strikingly, cisplatin treatment induced robust cleavage of gasdermin E (GSDME) (Fig. 4A), generating the active N-terminal fragment responsible for pyroptotic pore formation. This GSDME cleavage was concentration-dependent and observed in both CAL27 and HCT15 cell lines (Fig. 4A,B). As caspase-3-mediated cleavage of GSDME is a recognized mechanism for chemotherapy-induced pyroptosis [14,26,27], our findings position GSDME as the dominant executor of cisplatin-triggered pyroptosis in these models. To establish the functional contribution of GSDME-dependent pyroptosis to cisplatin cytotoxicity, we performed siRNA-mediated knockdown of GSDME. Successful GSDME silencing

significantly reduced both full-length and cleaved N-terminal GSDME protein levels (Fig. 4C). Critically, attenuation of GSDME expression markedly reduced cisplatin-induced cell death (Fig. 4D,E), demonstrating that GSDME cleavage is essential for a significant portion of cisplatin's cytotoxic effect. Collectively, these results demonstrate that cisplatin activates pyroptosis predominantly through the caspase-3/GSDME axis rather than the GSDMD pathway. This establishes GSDME cleavage as a key molecular switch converting apoptotic caspase-3 activation (Fig. 2) into pyroptotic cell death (Fig. 4), revealing intricate crosstalk between cisplatin-induced PCD pathways.

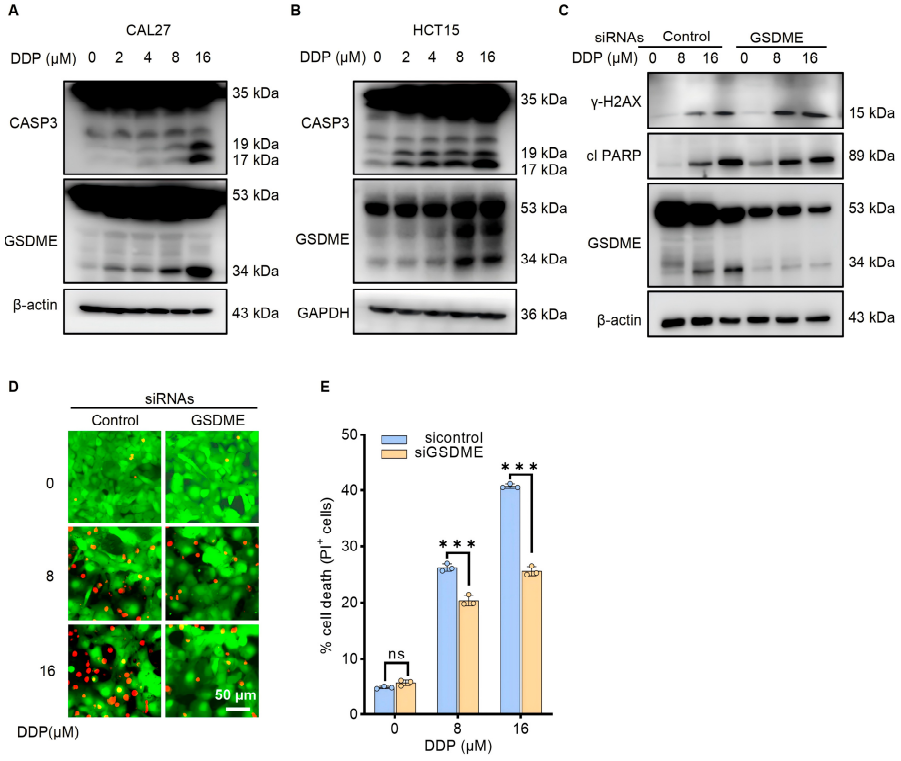

Figure 4: Cisplatin induces Pyroptosis. (**A**,**B**) Immunoblot analysis of CSAP3 activation, pro-(P53) and activated (P34) GSDME in CAL27 cells (**A**) and HCT15 cells (**B**) after cisplatin treatment (48 h). (**C**) Immunoblotting of GSDME-WT and GSDME-knockdown cells, to confirm GSDME downregulation. CAL27 cells were transfected with control siRNA or GSDME siRNA, and treated with 0 μM, 8 μM, or 16 μM cisplatin for 36 h. (**D**) Knocking down GSDME reduced the occurrence of cell death. Red indicates dead cells, while green represents live cells. Scale bar, 50 μm. (**E**) Quantification of cell death from D. n.s. $p > 0.05$, $^{***}p < 0.001$ (Student's t test, n = 3).

3.5 Cisplatin Induces Ferroptosis through ROS Accumulation and Lipid Peroxidation

Beyond apoptosis, necroptosis, and pyroptosis, we investigated cisplatin's potential to trigger ferroptosis, an iron-dependent form of regulated cell death driven by lethal accumulation of lipid peroxides, first defined in 2012 [28]. Ferroptosis arises from dysregulated iron metabolism, mitochondrial dysfunction, and imbalances in polyunsaturated fatty acid phospholipid (PUFA-PL) synthesis/peroxidation, culminating in overwhelming lipid peroxidation. We first assessed reactive oxygen species (ROS) accumulation, a key upstream event promoting ferroptosis. Using the DCFH-DA probe, we observed a significant increase in intracellular ROS levels in CAL27 cells following 24-h cisplatin treatment (Fig. 5A,B). While cancer cells typically exhibit elevated baseline ROS [29], cisplatin further amplified this oxidative stress in a dose-dependent manner. Critically, cisplatin treatment triggered profound lipid peroxidation, the hallmark

executor of ferroptosis. Using a fluorescent lipid peroxidation sensor (exhibiting an oxidation-dependent spectral shift from red to green), we detected significant dose-dependent increases in lipid peroxidation after 24-h treatment with 8 μM or 16 μM cisplatin compared to controls (Fig. 5C,D). This cisplatin-induced lipid peroxidation was completely abrogated by pretreatment with the potent ferroptosis inhibitor ferrostatin-1 (Fer-1, 10 μM), confirming its specificity (Fig. 5C,D).

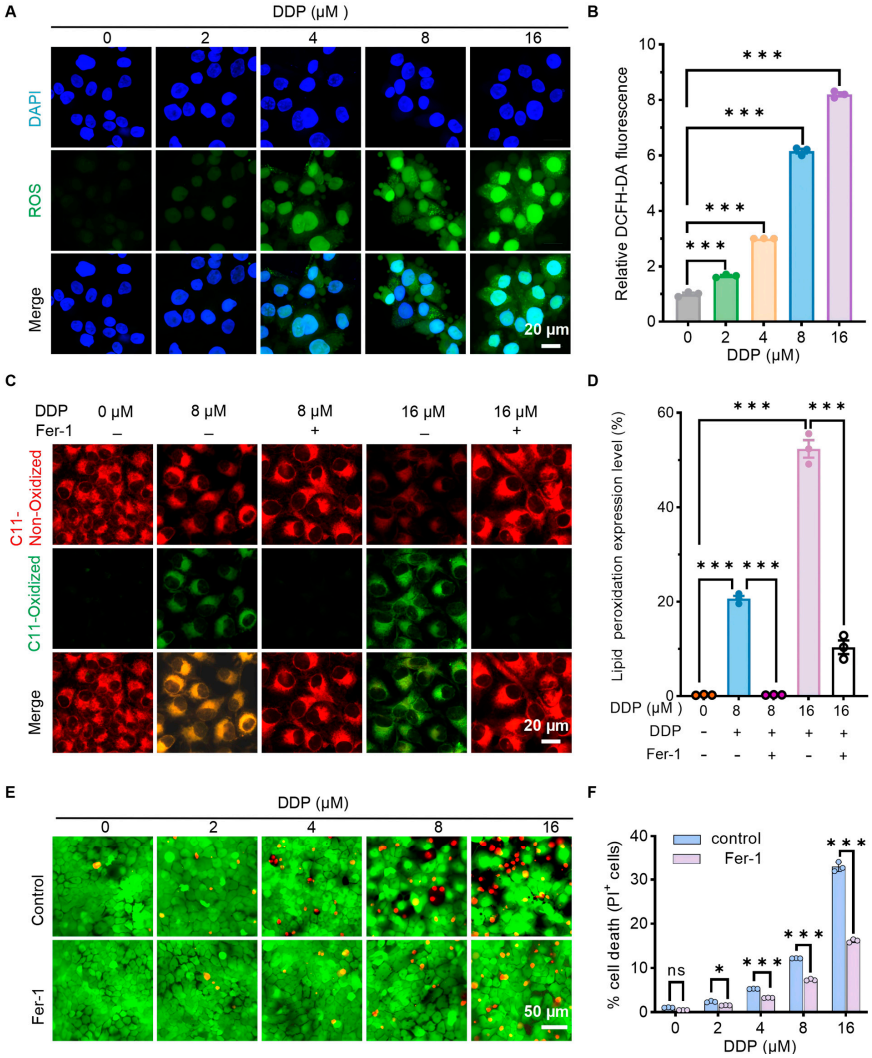

Figure 5: Cisplatin induces Ferroptosis. (**A**) Fluorescent images depicting DCFH-DA (green) and nuclear DNA (blue) in CAL27 cells were detected after cisplatin treatment for 24h at 0 μM, 2 μM, 4 μM, 8 μM, or 16 μM. Scale bar, 20 μm. (**B**) Relative fluorescence intensity of DCFH-DA. ***$p < 0.001$ (one-way ANOVA with multiple comparisons, n = 3). (**C**) Representative images of immunofluorescence staining of lipid peroxidation by the C11-BODIPY 581/591 probe. CAL27 cells were treated with 0 μM, 8 μM, or 16 μM cisplatin for 24 h, or exposed for 24 h after pretreatment with the ferroptosis inhibitor Fer-1 (10 μM) for 2 h. Green represents oxidation, while red represents non-oxidation. Scale bar, 20 μm. (**D**) The fluorescence intensity in C was quantified with Fiji software. ***$p < 0.001$ (one-way ANOVA multiple comparisons test, n = 3). (**E**) Representative images of cell death and (**F**) quantification of cell death in CAL27 cells treated with 0 μM, 2 μM, 4 μM, 8 μM, or 16 μM cisplatin in the presence or absence of a ferroptosis inhibitor, 10 μM Fer-1, for 48 h. Red indicates dead cells, while green represents live cells. Scale bar, 50 μm. n.s. $p > 0.05$, *$p < 0.05$, ***$p < 0.001$ (student's t test, n = 3).

To functionally establish ferroptosis's contribution to cisplatin cytotoxicity, we performed rescue experiments with Fer-1. Pretreatment with Fer-1 (10 μM, 2 h) significantly attenuated cisplatin-induced cell death after 48 h (Fig. 5E,F). This protective effect was dose-dependent, becoming statistically significant at cisplatin concentrations ≥4 μM. Importantly, Fer-1 similarly rescued cisplatin-induced death in HCT15 cells (Supplementary Fig. S3A,B), demonstrating broader relevance. Collectively, these results demonstrate that cisplatin activates ferroptosis through ROS overproduction and subsequent iron-dependent lipid peroxidation. This pathway significantly contributes to cisplatin cytotoxicity, particularly at intermediate-to-high concentrations, and is pharmacologically targetable.

3.6 Cisplatin Induces Multi-PCD Pathways in Tumor Xenografts

To validate whether cisplatin's capacity to induce multiple programmed cell death (multi-PCD) pathways extends to *in vivo* settings, we performed a comprehensive H&E and IHC analysis on xenograft tumors from cisplatin-treated mice. Mice bearing CAL27-derived tumors (~100 mm^3) received cisplatin (1 mg/kg or 4 mg/kg) or vehicle weekly for three weeks. Cisplatin treatment significantly reduced final tumor volumes compared to controls (Supplementary Fig. S4A), consistent with its therapeutic efficacy and in line with *in vitro* observations, it also led to decreased tumor cell proliferation and increased DNA damage in mouse tumors (Supplementary Fig. S4B,C). As shown in Fig. 6A, $Ki67^+$ proliferating cells were dramatically reduced, and γ-$H2AX^+$ DNA damage cells were increased concurrently, suggesting that DNA damage drives growth arrest. Critically, all four PCD pathways were co-activated in cisplatin-treated tumors. Elevated cleaved caspase and increased $pMLKL^+$ cells were indicators for induced apoptosis and necroptosis, respectively. Meanwhile, enhanced GSDME cell membrane (mGSDME) expression and accumulation of 4-HNE adducts were indicators for activated pyroptosis and ferroptosis, respectively.

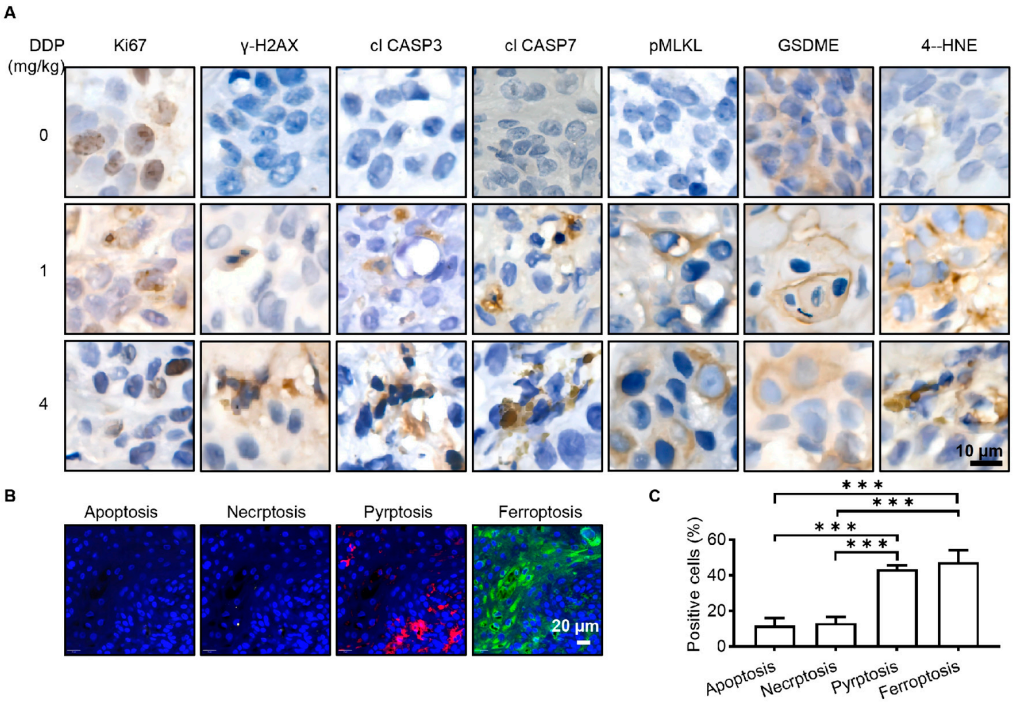

Figure 6: *Cont.*

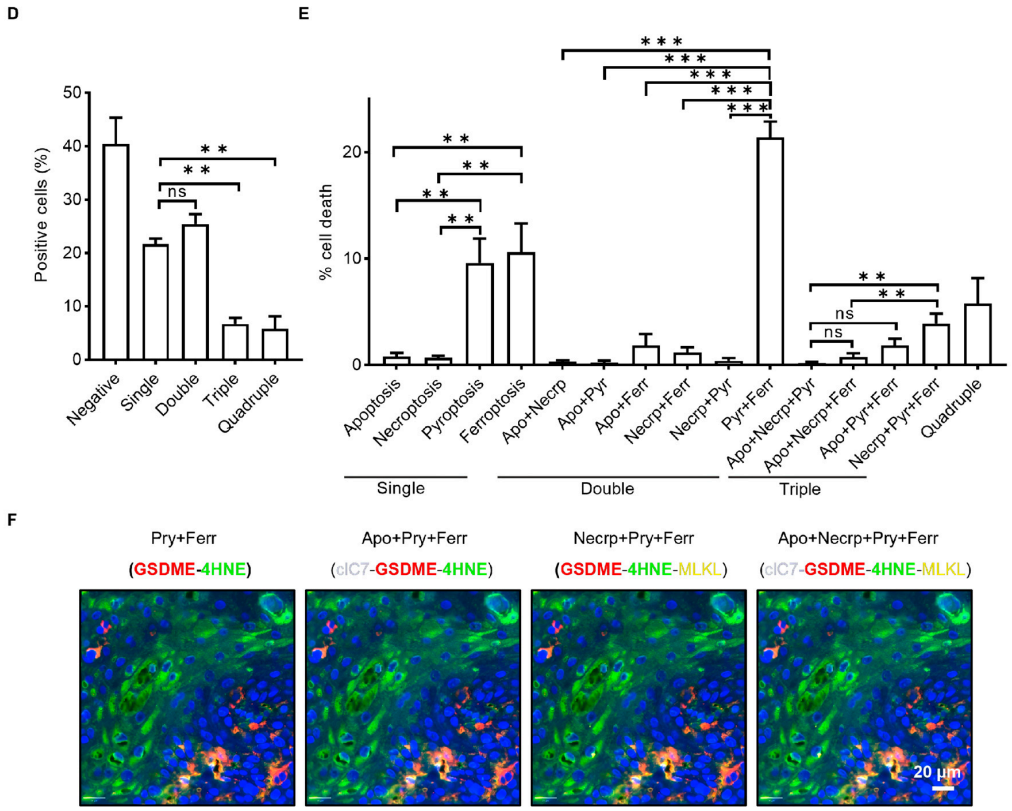

Figure 6: Immunohistochemical and multiplex immunofluorescence analysis of programmed cell death in tumor tissue. (**A**) Representative immunohistochemical staining of tumor tissue sections for Ki67, γ-H2AX, cleaved caspase-3, cleaved caspase-7, pMLKL, GSDME, and 4-HNE (n = 3). Scale bars represent 10 μm. (**B**) Representative tumor tissue stained with cleaved caspase-7 (clC7), MLKL, GSDME, 4-HNE, indicating apoptosis, necroptosis (mMLKL), pyroptosis (mGSDME), and ferroptosis, respectively. Scale bars represent 20 μm. (**C**) Quantitative results for B: individual statistical analysis of each molecular marker. $^{***}p < 0.001$ (one-way ANOVA multiple comparisons test). (**D**,**E**) Detailed statistical results of various cell death types from B Single indicates expression of one cell death marker, dual indicates two cell death markers, triple indicates three, and quadruple indicates four distinct cell death markers. n.s. $p > 0.05$, $^{**}p < 0.01$, $^{***}p < 0.001$ (one-way ANOVA multiple comparisons test). (**F**) Representative images of multiple death-type combinations are presented, as determined by the quantitative analyses in B and E. Scale bars represent 20 μm.

To systematically evaluate the relative contributions of distinct programmed cell death pathways in cisplatin's antitumor efficacy, we performed CmTSA staining on xenograft tumor tissues from the 4 mg/kg cisplatin-treated group. Quantitative analysis (Fig. 6B–D) revealed that cisplatin induced activation of multiple PCD modalities in tumor cells. Comprehensive evaluation of four PCD pathways further suggests that pyroptosis and ferroptosis are prominently involved (Fig. 6C). Subgroup analysis of single PCD types (Fig. 6E) identified pyroptosis (mGSDME) and ferroptosis (4-HNE+) as the predominant modalities. This pattern persisted in dual PCD analysis, where pyroptosis-ferroptosis co-existence reached 21.4 ± 3.3%, significantly surpassing other combinations. Immunofluorescence co-localization (Fig. 6F) provided visual validation of their co-expression within tumor tissues, with distinct spatial overlap observed between mGSDME and 4-HNE markers. Collectively, these findings demonstrate that cisplatin synergistically activates multiple PCD pathways *in vivo*, where pyroptosis and ferroptosis represent frequently observed components of the tumor cell death response.

3.7 Enhanced Pyroptosis-Ferroptosis Co-Activation Characterizes Cisplatin Response in Clinical Specimens

To investigate cisplatin-induced multi-PCD in human tumors, we performed CmTSA on paired pre- and post-neoadjuvant cisplatin-based chemotherapy (NAC) specimens. Using pan-cytokeratin (pan-CK) for tumor cell identification, we quantified co-expression patterns of PCD markers. The results revealed the following changes in post-NAC tumor cells: (1) significant reduction in proliferative capacity (decreased Ki67 expression, $p < 0.001$, Fig. 7A,B), (2) increased expression of DNA damage markers (γ-H2AX, $p < 0.001$, Fig. 7A,B), and (3) upregulated expression of markers for death of multiple programmed cell death pathways (Fig. 7C,D). Quantitative analysis demonstrated significant alterations in tumor cell death patterns following NAC (Fig. 7E,F): (1) pyroptosis incidence was markedly increased in single cell death modality analysis ($p < 0.05$); (2) the proportion of tumor cells co-expressing pyroptosis marker GSDME and ferroptosis marker 4-HNE was significantly elevated in dual death type assessment ($p < 0.01$). Further investigation identified three characteristic co-expression patterns: apoptosis-pyroptosis-ferroptosis ($p < 0.01$), necroptosis-pyroptosis-ferroptosis triple death modality ($p < 0.01$), and quadruple cell death marker co-expression ($p < 0.01$; Fig. 7E–G). Consistent with prior animal studies, the co-activation of pyroptotic and ferroptotic markers was particularly prominent in NAC-treated tumors, which also showed an increased frequency of multi-PCD compared to pretreatment levels. These findings indicate that cisplatin treatment induces a characteristic multiple cell death phenotype in tumor cells, with particularly prominent co-activation of pyroptosis and ferroptosis pathways. This unique death modality crosstalk may not only represent a crucial molecular determinant of cisplatin's chemotherapeutic efficacy but also provide potential novel targets for therapeutic optimization.

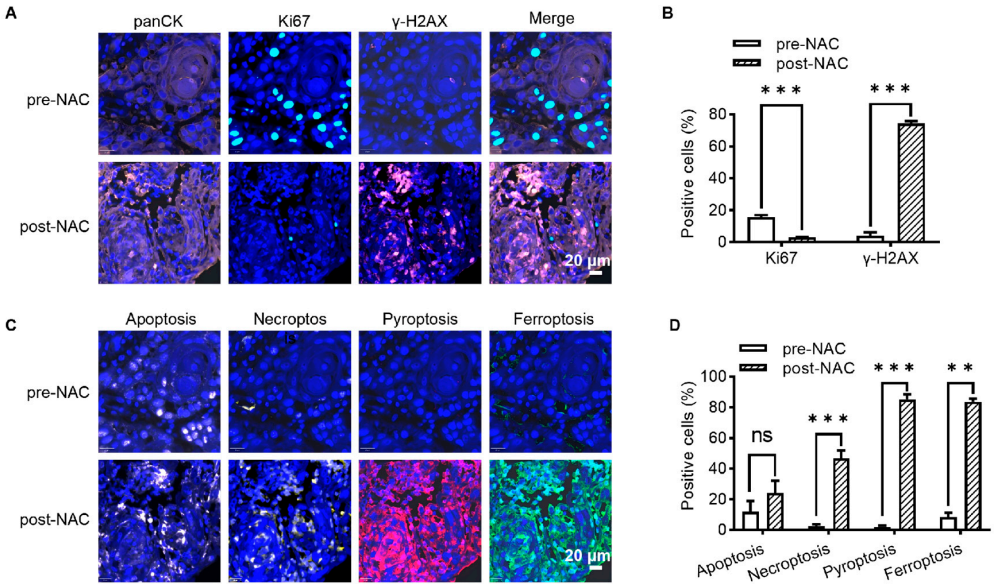

Figure 7: *Cont.*

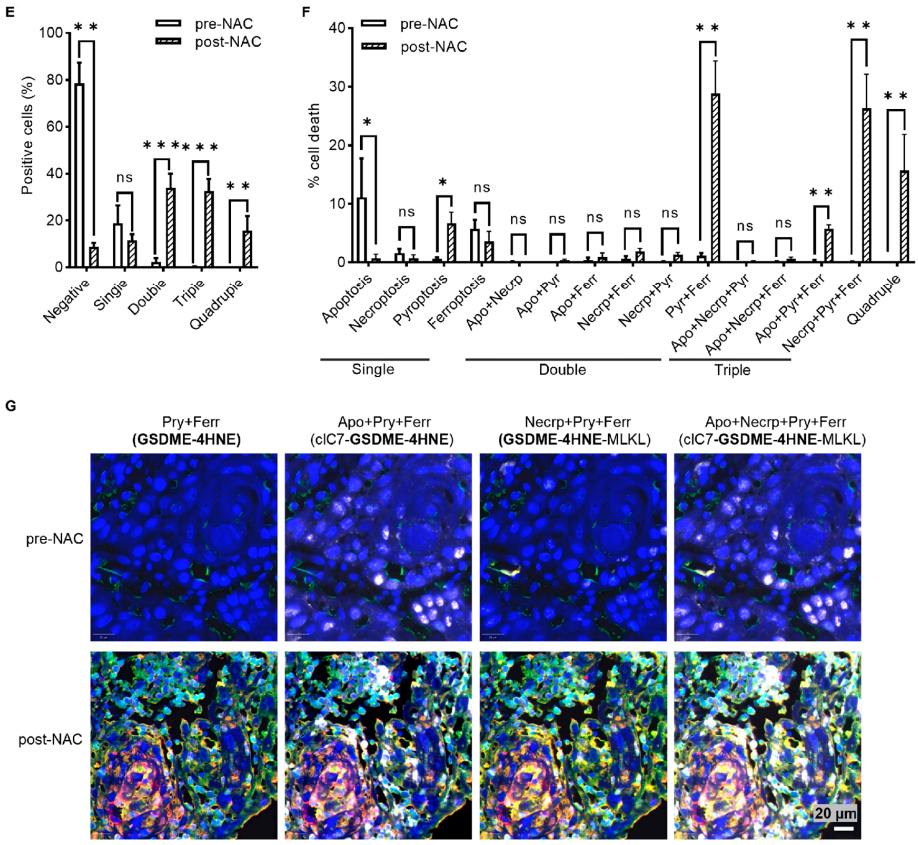

Figure 7: CmTSA analysis of m-PCD markers in pre-NAC and post-NAC specimens of OSCC. (**A**) Representative OSCC stained with three markers (pan-Cytokeratin (panCK), Ki67, γ-H2AX). Scale bars represent 20 μm. (**B**) Quantitative results for A: individual statistical analysis of each molecular marker (Student's *t* test). $^{***}p < 0.001$. (**C**) Representative OSCC stained with cleaved caspase-7 (clC7), MLKL, GSDME, 4-HNE, indicating apoptosis, necroptosis (mMLKL), pyroptosis (mGSDME), and ferroptosis, respectively. Scale bars represent 20 μm. (**D**) Quantitative results for C: individual statistical analysis of each molecular marker. n.s. $p > 0.05$, $^{**}p < 0.01$, $^{***}p < 0.001$ (student's *t* test). (**E**,**F**) Detailed statistical results of various cell death types from C. Single indicates expression of one cell death marker, dual indicates two cell death markers, triple indicates three, and quadruple indicates four distinct cell death markers. n.s. $p > 0.05$, $^{*}p < 0.05$, $^{**}p < 0.01$, $^{***}p < 0.001$ (student's *t* test). (**G**) Representative images of significantly overexpressed death-type combinations from F. Scale bars represent 20 μm.

4 Discussion

Our integrated study demonstrates that cisplatin induces a multi-PCD signature in tumor cells, which includes apoptosis, necroptosis, pyroptosis, and ferroptosis. This cell death response is dynamically regulated by drug dose and treatment duration. Notably, key pro-inflammatory modalities-pyroptosis and ferroptosis-were highly enriched in both preclinical models and patient samples, revealing a core pro-inflammatory axis in cisplatin's action.

The immunomodulatory potential of non-apoptotic PCD pathways represents a promising frontier for combinatorial therapy. Unlike non-inflammatory apoptosis, pyroptosis, necroptosis, and ferroptosis release damage-associated molecular patterns (DAMPs) and cytokines that stimulate antitumor immunity [30]. In our clinical specimens, markers of pyroptosis and ferroptosis pathways were striking enriched. This suggests that pyroptosis and ferroptosis are prominently involved and may constitute the core pro-inflammatory signaling axis in the cisplatin response (Fig. 7C,D). Cisplatin creates a ROS-rich microenvironment

conducive to ferroptosis, alongside lipid metabolism remodeling and iron regulation [31]. While ROS is a well-characterized mediator of cisplatin-induced cell death, it remains unclear whether its regulation of ferroptosis primarily depends on ROS activation. Simultaneously, caspase-3 activation by cisplatin not only executes apoptosis but also cleaves GSDME to trigger pyroptosis. The significant upregulation of GSDME-mediated pyroptosis *in vivo* positions GSDME as a molecular switch, steering cell death toward immunogenic pyroptosis over silent apoptosis and thereby shaping the tumor immune microenvironment.

Mechanistically, cisplatin preferentially activates the caspase-3/GSDME-dependent pyroptosis axis (Fig. 4), initiating a self-amplifying pro-inflammatory cascade: pyroptotic cells release tumor antigens prime cytotoxic T lymphocytes (CTLs) [32], while CTL-derived granzyme B cleaves GSDME to propagate further pyroptosis. This positive feedback loop amplifies antigen presentation and T-cell activation [33]. Concurrently, $CD8^+$ T cells modulate tumor ferroptosis during immunotherapy [34], and ferroptotic cells enhance T-cell infiltration [35], revealing bidirectional crosstalk between ferroptosis and adaptive immunity. This synergy between cisplatin-induced pyroptosis and ferroptosis and the resultant adaptive immune response provides a compelling mechanistic rationale for the observed clinical efficacy of combining cisplatin with immune checkpoint inhibitors. Elucidating this coordinated immunogenic cell death network is a major focus of our ongoing research.

Collectively, this study systematically uncovers the co-activation of multi-PCD modalities, notably pro-inflammatory ferroptosis and pyroptosis, following cisplatin-based chemotherapy. While distinct in their mechanisms, these PCD pathways exhibit coordinated pro-inflammatory properties. This provides the mechanistic foundation for the synergistic efficacy observed when combining cisplatin with immune checkpoint inhibitors. Furthermore, it establishes a framework for therapeutically modulating cisplatin-induced PCDs to preferentially amplify pro-inflammatory death pathways, thereby enhancing anti-tumor immunity and improving immunotherapy responses.

Although cisplatin induces the coordinated activation of multiple cell death programs, the functional contribution to cell death of each pathway has not yet been sufficiently validated. Moreover, whether immunogenic cell death pathways, rather than related deaths, particularly pyroptosis and ferroptosis, directly contribute to antitumor immune responses remains to be determined. Translating these mechanistic insights into therapeutic benefit may be enabled by advanced strategies such as programmable drug delivery systems [36,37]. Together, the convergence of mechanistic biology and translational engineering offers a promising framework for the development of optimized immunochemotherapeutic strategies.

5 Conclusions

This study systematically defines cisplatin as an orchestrator of multiple programmed cell death pathways across experimental and clinical contexts. Cisplatin induces apoptosis, necroptosis, pyroptosis, and ferroptosis, with preferential engagement of the pro-inflammatory pathways of pyroptosis and ferroptosis in tumors. These findings reposition cisplatin as a central regulator of multi-PCD networks and offer a new framework for designing rational multi-PCD-targeted therapies.

Acknowledgement: The authors thank all the staff of the State Key Laboratory of Oral Diseases at Sichuan University for their expert technical assistance and administrative support. We sincerely thank Dr Jian Jiang for providing the experimental site.

Funding Statement: This work was supported by the grants of the National Natural Science Foundations of China (NSFC; Grant Nos. 82170971, 82373187, 82273165); the Sichuan Science and Technology Program (Grant Nos. 2025NSFJQ0062 and 2024YFFK0293); the Scientific Research Foundation of the West China Hospital of Stomatology,

Sichuan University (RD-03-202110); and the Special Funding for the State Key Laboratory of Oral Diseases, Sichuan University (SKLOD-2025KP009).

Author Contributions: The authors confirm contribution to the paper as follows: Conceptualization, Xiaodong Feng, Xiaoping Xu and Ju Li; methodology, Ju Li, Pengcheng Rao, Dan Yang, Tong Zhou, Jianguo Gan, Die Lv, Shuting Zhou, Yang Peng, Jian Jiang; software, Ju Li, Dan Yang, Jianguo Gan, Die Lv, Shuting Zhou; validation, Yang Peng, Yuchen Jiang, Jian Jiang; formal analysis, Jianguo Gan, Die Lv, Yuchen Jiang; investigation, Ju Li, Pengcheng Rao, Dan Yang, Tong Zhou, Yuchen Jiang; resources, Xiaoqiang Xia, Qianming Chen, Xiaoping Xu, Xiaodong Feng; data curation, Ju Li, Pengcheng Rao, Jian Jiang, Xiaodong Feng; writing—original draft preparation, Ju Li; writing—review and editing, Xiaoqiang Xia, Xiaoping Xu, Xiaodong Feng; visualization, Yang Peng, Xiaoqiang Xia, Xiaoping Xu, Xiaodong Feng; supervision, Xiaoqiang Xia, Xiaoping Xu, Xiaodong Feng; project administration, Xiaoqiang Xia, Qianming Chen, Xiaoping Xu, Xiaodong Feng; funding acquisition, Qianming Chen, Xiaoping Xu, Xiaodong Feng. All authors reviewed and approved the final version of the manuscript.

Availability of Data and Materials: All data generated or analyzed during this study are included in this published article and its Supplementary Information Files. All primary data can be made available from the corresponding authors upon reasonable request.

Ethics Approval: The present study was approved by the Experimental Animal Ethics Committee of West China Hospital, Sichuan University (Ethics Approval No. 20220330002), and all experiments were conducted in compliance with the institutional ethical guidelines for animal experiments. Patient consent for publication: Not applicable. Human specimens were collected with approval from the Ethics Committee for Medical Research and New Medical Technology of Sichuan Cancer Hospital (Ethics Approval No. KY-2021-001-06), with full informed consent from the patient.

Conflicts of Interest: The authors declare no conflicts of interest.

Supplementary Materials: The supplementary material is available online at https://www.techscience.com/doi/10.32604/biocell.2026.075437/s1. Figure S1: CmTSA staining workflow. Figure S2: GSDME is essential in cisplatin-induced pyroptosis. Figure S3: Fer-1 inhibits cell death in HCT15 cells. Figure S4: H&E and multiplex immunofluorescence analysis of animal tumor tissues.

Abbreviations

PCD	programmed cell death
multi-PCD	multiple-programmed cell death
Fer-1	ferrostatin-1
NSA	necrosulfonamide
zLEHD	Z-LEHD-FMK TFA
PBS	phosphate-buffered saline
PFA	paraformaldehyde
PI	propidium iodide
SDS	sodium dodecyl sulfate
ECL	enhanced chemiluminescence
DCFH-DA	2,7-Dichlorodi-hydrofluorescein diacetate
H&E staining	Hematoxylin and eosin staining
IHC	Immunohistochemical
4-HNE	4-hydroxynonenal
OSCC	oral squamous cell carcinoma
CmTSA	Cyclic multiplexed tissue staining
NAC	neoadjuvant chemotherapy
TSA	tyramide signal amplification
IF	immunofluorescence
DDR	DNA damage response

cl PARP	cleaved PARP
CASP9	caspase-9
CSAP3	caspase-3
cl CASP7	cleaved caspase-7
RIPK3	receptor-interacting protein kinase 3
MLKL	mixed lineage kinase domain-like protein
GSDMD	gasdermin D
GSDME	gasdermin E
PUFA-PL	polyunsaturated fatty acid phospholipid
ROS	reactive oxygen species
pan-CK	pan-cytokeratin
clC7	cleaved caspase-7

References

1. Galanski MS. Recent developments in the field of anticancer platinum complexes. Recent Pat Anticancer Drug Discov. 2006;1(2):285–95. [CrossRef].
2. Patil V, Noronha V, Dhumal SB, Joshi A, Menon N, Bhattacharjee A, et al. Low-cost oral metronomic chemotherapy versus intravenous cisplatin in patients with recurrent, metastatic, inoperable head and neck carcinoma: an open-label, parallel-group, non-inferiority, randomised, phase 3 trial. Lancet Glob Health. 2020;8(9):e1213–22. [CrossRef].
3. Shi Z, Hao L, Han X, Wu Z, Pang K, Dong Y, et al. Targeting HNRNPU to overcome cisplatin resistance in bladder cancer. Mol Cancer. 2022;21(1):37. [CrossRef].
4. Vasan N, Baselga J, Hyman DM. A view on drug resistance in cancer. Nature. 2019;575(7782):299–309. [CrossRef].
5. Marine JC, Dawson SJ, Dawson MA. Non-genetic mechanisms of therapeutic resistance in cancer. Nat Rev Cancer. 2020;20(12):743–56. [CrossRef].
6. Riddell IA. Cisplatin and oxaliplatin: our current understanding of their actions. Met Ions Life Sci. 2018;18:books–9783110470734. [CrossRef].
7. Pu Y, Li L, Peng H, Liu L, Heymann D, Robert C, et al. Drug-tolerant persister cells in cancer: the cutting edges and future directions. Nat Rev Clin Oncol. 2023;20(11):799–813. [CrossRef].
8. Kerr JF, Wyllie AH, Currie AR. Apoptosis: a basic biological phenomenon with wide-ranging implications in tissue kinetics. Brit J Cancer. 1972;26(4):239–57. [CrossRef].
9. Park W, Wei S, Kim BS, Kim B, Bae SJ, Chae YC, et al. Diversity and complexity of cell death: a historical review. Exp Mol Med. 2023;55(8):1573–94. [CrossRef].
10. Green DR. The coming decade of cell death research: five riddles. Cell. 2019;177(5):1094–107. [CrossRef].
11. Yuan J, Ofengeim D. A guide to cell death pathways. Nat Rev Mol Cell Biol. 2024;25(5):379–95. [CrossRef].
12. Luo R, Onyshchenko K, Wang L, Gaedicke S, Grosu AL, Firat E, et al. Necroptosis-dependent immunogenicity of cisplatin: implications for enhancing the radiation-induced abscopal effect. Clin Cancer Res. 2023;29(3):667–83. [CrossRef].
13. Ruhl D, Du TT, Wagner EL, Choi JH, Li S, Reed R, et al. Necroptosis and apoptosis contribute to cisplatin and aminoglycoside ototoxicity. J Neurosci. 2019;39(15):2951–64. [CrossRef].
14. Wang Y, Gao W, Shi X, Ding J, Liu W, He H, et al. Chemotherapy drugs induce pyroptosis through caspase-3 cleavage of a gasdermin. Nature. 2017;547(7661):99–103. [CrossRef].
15. Zhou Z, Zhao Y, Chen S, Cui G, Fu W, Li S, et al. Cisplatin promotes the efficacy of immune checkpoint inhibitor therapy by inducing ferroptosis and activating neutrophils. Front Pharmacol. 2022;13:870178. [CrossRef].
16. Mei H, Zhao L, Li W, Zheng Z, Tang D, Lu X, et al. Inhibition of ferroptosis protects House Ear Institute-Organ of Corti 1 cells and cochlear hair cells from cisplatin-induced ototoxicity. J Cell Mol Med. 2020;24(20):12065–81. [CrossRef].
17. Cheng K, Li X, Lv W, Zhao G, Zhou R, Chang C, et al. Spatial interactions of immune cells as potential predictors to efficacy of toripalimab plus chemotherapy in locally advanced or metastatic pancreatic ductal adenocarcinoma: a phase Ib/II trial. Signal Transduct Target Ther. 2024;9(1):321. [CrossRef].

18. Tyagi A, Kaushal K, Chandrasekaran AP, Sarodaya N, Das S, Park CH, et al. CRISPR/Cas9-based genome-wide screening for deubiquitinase subfamily identifies USP1 regulating MAST1-driven cisplatin-resistance in cancer cells. Theranostics. 2022;12(13):5949–70. [CrossRef].
19. Low HB, Wong ZL, Wu B, Kong LR, Png CW, Cho YL, et al. DUSP16 promotes cancer chemoresistance through regulation of mitochondria-mediated cell death. Nat Commun. 2021;12(1):2284. [CrossRef].
20. Ayoub N, Jeyasekharan AD, Bernal JA, Venkitaraman AR. HP1-beta mobilization promotes chromatin changes that initiate the DNA damage response. Nature. 2008;453(7195):682–6. [CrossRef].
21. Tang D, Kang R, Vanden Berghe T, Vandenabeele P, Kroemer G. The molecular machinery of regulated cell death. Cell Res. 2019;29(5):347–64. [CrossRef].
22. Van Opdenbosch N, Lamkanfi M. Caspases in cell death, inflammation, and disease. Immunity. 2019;50(6):1352–64. [CrossRef].
23. Kashyap D, Garg VK, Goel N. Intrinsic and extrinsic pathways of apoptosis: role in cancer development and prognosis. Adv Protein Chem Struct Biol. 2021;125:73–120. [CrossRef].
24. Sun L, Wang H, Wang Z, He S, Chen S, Liao D, et al. Mixed lineage kinase domain-like protein mediates necrosis signaling downstream of RIP3 kinase. Cell. 2012;148(1–2):213–27. [CrossRef].
25. Broz P, Pelegrín P, Shao F. The gasdermins, a protein family executing cell death and inflammation. Nat Rev Immunol. 2020;20(3):143–57. [CrossRef].
26. Wang S, Zhang MJ, Wu ZZ, Zhu SW, Wan SC, Zhang BX, et al. GSDME is related to prognosis and response to chemotherapy in oral cancer. J Dent Res. 2022;101(7):848–58. [CrossRef].
27. Rogers C, Fernandes-Alnemri T, Mayes L, Alnemri D, Cingolani G, Alnemri ES. Cleavage of DFNA5 by caspase-3 during apoptosis mediates progression to secondary necrotic/pyroptotic cell death. Nat Commun. 2017;8(1):14128. [CrossRef].
28. Dixon SJ, Lemberg KM, Lamprecht MR, Skouta R, Zaitsev EM, Gleason CE, et al. Ferroptosis: an iron-dependent form of nonapoptotic cell death. Cell. 2012;149(5):1060–72. [CrossRef].
29. Cheung EC, Vousden KH. The role of ROS in tumour development and progression. Nat Rev Cancer. 2022;22(5):280–97. [CrossRef].
30. Zheng Y, Sun L, Guo J, Ma J. The crosstalk between ferroptosis and anti-tumor immunity in the tumor microenvironment: molecular mechanisms and therapeutic controversy. Cancer Commun. 2023;43(10):1071–96. [CrossRef].
31. Stockwell BR. Ferroptosis turns 10: emerging mechanisms, physiological functions, and therapeutic applications. Cell. 2022;185(14):2401–21. [CrossRef].
32. Wang S, Liu Y, Zhang L, Sun Z. Methods for monitoring cancer cell pyroptosis. Cancer Biol Med. 2021;19(4):398–414. [CrossRef].
33. Fournel L, Wu Z, Stadler N, Damotte D, Lococo F, Boulle G, et al. Cisplatin increases PD-L1 expression and optimizes immune check-point blockade in non-small cell lung cancer. Cancer Lett. 2019;464:5–14. [CrossRef].
34. Wang W, Green M, Choi JE, Gijón M, Kennedy PD, Johnson JK, et al. $CD8^+$ T cells regulate tumour ferroptosis during cancer immunotherapy. Nature. 2019;569(7755):270–4. [CrossRef].
35. Li X, Li Y, Tuerxun H, Zhao Y, Liu X, Zhao Y. Firing up “cold” tumors: ferroptosis causes immune activation by improving T cell infiltration. Biomed Pharmacother. 2024;179:117298. [CrossRef].
36. Shi W, Xi Y, Sheng X, Das S, He D, Collins K, et al. Injectable hydrogels for programmable nanoparticle release. Adv Funct Mater. 2025;35(1):2409796. [CrossRef].
37. Huang Y, Wei D, Wang B, Tang D, Cheng A, Xiao S, et al. NIR-II light evokes DNA cross-linking for chemotherapy and immunogenic cell death. Acta Biomater. 2023;160:198–210. [CrossRef].